Life Beyond Diffraction: Opening New Routes to Materials Characterization with Next-Generation Optical Near-Field Approaches

P. James Schuck, Alexander Weber-Bargioni,* Paul D. Ashby, D. Frank Ogletree, Adam Schwartzberg, and Stefano Cabrini**

Near-field optical microscopies and spectroscopies seek to investigate materials by combining the best aspects of optical characterization and scan-probe microscopy techniques. In principle, this provides access to chemical, morphological, physical and dynamical information at nanometer length scales that is impossible to access by other means. But a number of challenges, particularly on the scan-probe front, have limited the widespread application of near-field investigations. This work describes how recent probe engineering and technique innovation have addressed many of these challenges. This Feature Article begins with a short overview of the field, providing perspective and motivation for these developments and highlighting some key improvements. This is followed by a more in-depth description of the near-field advances developed at the Molecular Foundry, a national nanoscience User Facility–advances that provide groundwork for generally-applicable nano-optical studies. Finally, a discussion is provided of what progress is still needed in order to realize the ultimate objective of translating all optical measurements to the nanoscale.

1. Introduction

Recent advances in nanoscience, particularly in the design of novel nanostructured materials, have highlighted the need for spectroscopic characterization techniques that provide chemical information along with true nanoscale spatial resolution. Scanning probe microscopy (SPM), starting with the development of scanning tunneling microscopy (STM) in the early 1980s, has been a transformative tool for understanding surface and interface morphology, electronic structure and chemistry down to the sub-atomic scale. However, obtaining molecular-level chemical information and probing dynamics at ultrafast time-scales with SPM has remained challenging. While these are precisely the strengths of optical methods, optical spatial resolution has generally been restricted by the diffraction limit. Thus, a major materials science (and nanoscience) goal is to unlock previously inaccessible physics and dynamics*at relevant length scales* within materials systems by combining the chemical information and ultrafast temporal resolution (fs) inherent in optical studies with the capabilities of modern scanning probe techniques.[1,2]

Working towards this goal has been the primary aim of near-field scanning optical microscopy (NSOM). Over the years, a number of NSOM approaches have been developed. To give proper perspective and motivation for our work, we briefly review a few of the key approaches here. We have divided NSOM into three general classes (though in principle there are many variations), organized by the type of near-field probe employed: nano-aperture-based techniques; methods using sharp tips acting as optical transducers; and strategies based on advanced tip designs that involve more sophisticated optical antenna and/or structured apertures (discussed in more detail in Section 2.3), incorporating concepts from the field of plasmonics.

Before discussing NSOM, we note that a number of non-tip-based optical "super-resolution" microscopy approaches have been developed. These micro(nano)scopies, which include photon localization (e.g., photoactivated localization microscopy (PALM)[3,4]) and stimulated emission depletion (STED)[5] methods, are complementary to those described in this work. Because they are based on more-standard optical microscopy instrumentation and allow imaging in three dimensions, they have resulted in a recent revolution in bio-imaging.[6] However, these techniques rely on fluorescent/luminescent labeling of the sample, thus restricting the chemical and native-state information that can be obtained. NSOM methods, on the other hand, are surface techniques and have the ability to spectroscopically probe materials at nanometer length scales in their native, label-free state.

Perhaps still the most common NSOM approach makes use of conventional aperture-based probes.[7] These probes consist of metal-coated tapered dielectric waveguide structures with a resolution-defining sub-wavelength aperture in the metal coating at the apex: some of the light traveling down the waveguide leaks out the (nanoscale) aperture, creating a light spot that, very near the aperture, has a size defined by the aperture

Dr. P. J. Schuck, Dr. A. Weber-Bargioni, Dr. P. D. Ashby, Dr. D. F. Ogletree, Dr. A. Schwartzberg, Dr. S. Cabrini
Lawrence Berkeley National Lab
The Molecular Foundry, 1 Cyclotron Road Mail Stop, Berkeley, CA 94720, USA
E-mail: pjschuck@lbl.gov; afweber-bargioni@lbl.gov; scabrini@lbl.gov

DOI: 10.1002/adfm.201203432

diameter and not by the wavelength of the light. By scanning this aperture over a surface, it is possible to build up an optical image with resolution determined by the aperture diameter. Several review articles and texts have been written on this subject; readers interested in more details are directed to[1,7] and references therein. The idea for aperture-based sub-diffraction-limited optical imaging originated with Synge[8] in 1928, though the first experimental results at optical frequencies were not published until 1984 by Pohl et al.[9] and Lewis et al.[10] Approximately eight years later, the first fluorescence images of single molecules were acquired using aperture NSOM.[11] In the most widely-adapted approach, a fiber probe–consisting of a metal-coated tapered optical fiber with the small aperture at the apex–is raster-scanned over the sample while maintaining a small tip-sample distance.[12]

From a practical standpoint, however, this approach presents many complications. While aperture probes enable "background-free" imaging, where sample illumination occurs only within the nanoscale light spot created by the aperture probe, the boundary conditions for this type of waveguiding tip unfortunately demand that all propagating modes within the taper get cut off before reaching the aperture. This causes only evanescent waves to leak out from the end (see **Figure 1**).[13] Also, there is not significant local electric field enhancement at the aperture. These factors ultimately result in low optical throughput and signal strength.[13,14] In addition, because throughput is inversely proportional to the fourth power of the aperture radius,[14] signal-to-noise considerations in aperture NSOM ultimately constrain aperture size, and resolution, to ≈50–100 nm. In typical operation, the sample is either locally excited with the aperture tip while the emitted, scattered, or transmitted light is collected with a microscope objective, or the reverse. Because of the low optical throughput of aperture NSOM, it is generally prohibitive to both excite and collect through the aperture.

In fact, the general challenge for all NSOM methods has been in transducing propagating far-field radiation modes to evanescent, localized near-field modes at the end of a scan-probe tip, and vice-versa. Researchers have realized that this can at least partially be addressed by exploiting the collective response of free electrons in metals, i.e., by using surface plasmon polariton (SPP) resonances. In metals, particularly nanostructured metals, these resonances can couple with electromagnetic radiation to create fields that oscillate at optical frequencies while also being extremely localized and enhanced.[1]

Conventional aperture probes do not significantly exploit plasmon properties, limiting resolution and signal level, which has led to the development of other NSOM methods. Before discussing these, it is useful to list the properties of an *ideal* near-field probe: it would provide nanoscale resolution, efficient far-field to near-field (photonic-to-plasmonic) coupling, strong local optical field enhancement, and perhaps most importantly, it would be reproducible and robust. In addition, it would allow for background-free operation, control over near-field polarization, and independence from sample and substrate requirements–all while operating over a wide range of frequencies without sacrificing the field strength or throughput often associated with resonant structures (where enhancement and throughput is significant only for a small wavelength range). Compatibility with existing instrumentation would also be convenient, though it is not required. Not surprisingly, creating NSOM probes and instrumentation combining all these attributes has proven difficult.

Dr. P. James Schuck is a Staff Scientist and Director of the Imaging and Manipulation of Nanostructures Facility at the Molecular Foundry, located at Lawrence Berkeley National Lab. He earned his B.A. in Physics at UC Berkeley and his Ph.D. in Applied Physics at Yale University, followed by postdoctoral work at Stanford University, where he studied optical nanoantennas and single-molecule spectroscopy. Schuck's current research focuses on nanoscale spectroscopic investigations of condensed matter and bio-related materials.

Dr. Alexander Weber-Bargioni graduated from the University of Konstanz, received his PhD in physics from the University of British Columbia (2007), and did his postdoc at the Lawrence Berkeley National Laboratory. He is a staff scientist at the Molecular Foundry (LBNL), focusing on understanding and controlling fundamental optoelectronic processes at their respective length and time scale, utilizing advancements in plasmonics, near field imaging, and electronic structure and transport studies with molecular scale resolution.

Dr. Stefano Cabrini has been Director of the Nanofabrication Facility at the Molecular Foundry at LBNL since 2006. He received his Laurea degree in Physics from the University of Rome La Sapienza in 1991. He has over 15 year experience and over 100 publications in the field of nanofabrication. Dr. Cabrini's current research focuses on nanophotonics and metamaterials and in the development of new lithographic tools.

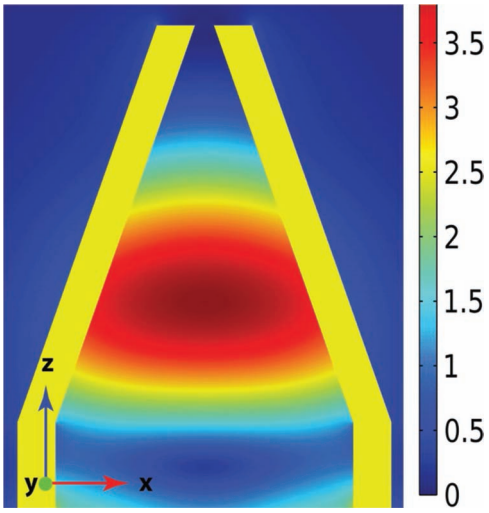

Figure 1. The cross section through a traditional cone-like aperture-based NSOM probe and the steady-state electric field normalized to the amplitude of the incident field for a linearly polarized E_x wave. For this simulation, $\lambda_o = 667$ nm was used.

As noted above, obtaining usable signal levels in NSOM investigations of materials is constrained by the (in)efficiency of any near-field probe in coupling far-field radiation to/from the near-field. There is also a more fundamental problem in acquiring satisfactory signal levels in nano-optical imaging and spectroscopy studies: as the optical probe volume is reduced to the nanoscale, the probe interacts with much less of the sample at any given time. It is in this context that apertureless NSOM (a-NSOM) approaches were developed. In a-NSOM, the nanoscale aperture is replaced by a much smaller particle or sharp tip of a scan-probe, which then serves as a *source* of locally-enhanced optical fields.[1] The resolution of this technique is now limited by the radius of curvature of the sharp tip or nanoparticle, typically ≈10 nm, as opposed to conventional aperture-based NSOM, where resolution is determined by the size of the aperture–typically ≈100 nm in most experiments. The enhanced fields at the end of an a-NSOM probe are used to excite signal from a nanoscopic volume in the sample, and locally emitted/scattered light is transduced to far-field radiation with the probe and detected directly. The enhanced local fields at the tip apex originate mostly from two effects: the "lightning rod effect", which is related to the geometric concentration of charge/polarization within an object in an electric field (see, for example, refs. [15] and [16]); and the optical excitation of SPPs on a metallic tip.[17] In the latter case, the tip bridges the momentum mismatch between electrons and photons, enabling coupling to SPPs. Often, it is the existence of nanoscale features and roughness on the metal tip that lead to this light-SPP coupling. Once created, SPPs over a broad spectral range can propagate toward the tip apex, where they are adiabatically compressed and focused by the conical taper into the apex region.[18–22]

By using a tip apex as a source of local excitation, a-NSOM has been employed for a wide range of optical spectroscopy measurements including linear[23–25] and multiphoton fluorescence,[26] spontaneous Raman[27–29] and coherent anti-Stokes Raman scattering (CARS)[30]—all with resolution of ≈10 nm. Using a-NSOM for local vibrational spectroscopy is particularly interesting as it provides molecular-level chemical specificity, as well as other structural information such as chemical bond orientation, strain,[31–33] structural inhomogeneities, and sample phase and crystallography.[34]

But despite yielding valuable insights into local material and chemical properties, results from many a-NSOM experiments have proven inconsistent, even when performed on nominally similar samples.[35] One practical cause of this irreproducibility is that a single sharp tip or nanoparticle-based tip is actually a non-ideal optical antenna. Because of the use of these somewhat crude antennas, near-field enhancement at the tip apex is often relatively small, and depends significantly on nanoscale features and details of the tip. Perhaps more importantly, weak field enhancement greatly limits the samples that can be studied to those that provide strong optical signal (i.e., those with large, often resonant, absorption or scattering cross-sections).

Improving the near-field signal-to-noise ratio is the primary issue addressed by scattering-type NSOM (s-NSOM), one of the more successful nano-optical modalities developed to date. This approach, based on a-NSOM instrumentation and concepts, uses a metal nanoparticle or sharp tip of a scan-probe as a field-concentrating scattering center:[36–41] The tip again acts as an optical antenna, reporting on local fields and light-matter interactions near a sample surface by scattering the localized modes into the far field for collection. The s-NSOM technique's success is rooted in the use and development of modulation methods that allow for the effective discrimination and amplification of the near-field signal at the detector. These methods, which include homodyne and "pseudoheterodyne" amplification, greatly increase the signal-to-noise ratio by interferometrically mixing the relatively weak near-fields with light from the excitation source.[42–44] Doing so can result not only in strong signal amplitudes and effective discrimination of near-field vs. far-field signal, but also in the determination of the phase of the near-field light. This has led s-NSOM to become a very powerful nano-characterization technique: it not only allows one to interrogate and map the vector field distributions surrounding optical structures with ≈10 nm resolution,[45–53] but to obtain and map nanoscale chemical information by observing changes in scattered light at wavelengths corresponding directly to vibrational or electronic transitions in the sample.[54–57] Recently, researchers have shown that it is possible to obtain full Fourier-transform infrared (FTIR) spectra at each pixel in an s-NSOM image (i.e., to perform nano-FTIR hyperspectral imaging).[58] In fact, microscope systems with this capability are now commercially available.

However, there is a major limitation to s-NSOM: only *elastically* scattered near-field light can be amplified using the modulation methods. This restricts the types of nano-optical spectroscopies and imaging that can be performed. More specifically, optical spectroscopies that use e.g., luminescence or Raman scattering to obtain important sample information are not amenable to this technique. In other words, a wide range of important material properties are not accessible with s-NSOM.[42]

2. Results and Discussion

Creating probes based on more-optimized optical antenna geometries that provide much larger enhancements and coupling efficiencies are essential for applying near-field techniques more generally and for expanding them beyond their current niche roles in nanoscience.

It is well-known from surface-enhanced Raman spectroscopy (SERS) that plasmonic fields are strongest in nanogap-like regions between plasmonically-coupled structures.[59–66] Therefore, some of the largest signals in tip-enhanced Raman spectroscopy (TERS) originate from tips exhibiting surface roughness and a SERS-like "hot-spot" at the apex.[67] But although the surface roughness enhances both light-SPP coupling efficiency and local fields in hot-spots, the random nature of the roughness leads to performance that is variable and not reproducible. More-optimal performance for a-NSOM occurs when intentionally exploiting the SERS effect through the so-called "tip-substrate gap mode" geometry. In the tip-substrate gap mode, a sharp metal tip is held ≈1 nm above a metallic substrate (with the sample located in the gap), effectively forming a vertically-oriented coupled dipole- or bowtie-like plasmonic antenna.[68–74] Recently, researchers have used the large field enhancements inherent in this geometry for full hyperspectral imaging of molecular and polymer layers, collecting a Raman spectrum at each image pixel with sub-second integration times.[72]

In practice, however, the operational requirements of tip-substrate gap mode limit its general applicability. It requires both a metallic substrate and a very small tip-substrate gap, meaning only very thin samples (e.g., molecular monolayers) can be investigated. The highest enhancements result when the light is polarized in the "z" direction normal to the sample surface, restricting one of the most useful variable parameters in Raman studies - the probed polarization.

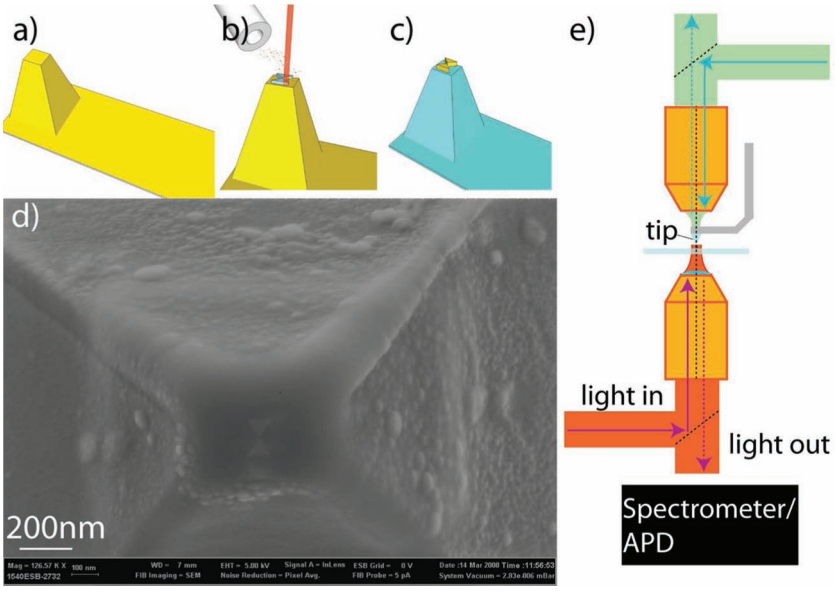

Figure 2. Bowtie antenna fabricated on AFM tip apex. The induced deposition mask lithography process is shown in (a–c), where a) the FIB-flattened tip is coated with 20 nm Au, b) bowtie masks are placed via E-Beam Induced Deposition and c) the mask is transferred via argon ion sputtering, resulting in d) a well defined optical Au antenna on an AFM tip apex. e) The tip is then placed into a near-field optical microscope where the optical axes of both objectives can be aligned with the near-field scanning probe tip. Here the tip was excited and the signal collected with the lower 1.4 NA oil objective.

2.1. Optical Bowtie Antenna-Based Probes for Enhanced Nano-Raman Spectroscopy

A solution to the problems with tip-substrate gap-mode is to engineer coupled optical antenna structures,[75,76] i.e., optical antennas with a small gaps,[77] directly on the scan-probe tip.[78,79] The antennas may be excited by far-field free-space optics, in scattering mode, or by coupling them to waveguides. Initial efforts along these lines had been hindered by fabrication constraints, but recent advances have made it possible to reliably create such next-generation probes.[80–84] Details about the innovations and progress in nano-optical scan-probe engineering can be found, for example in ref. [85]. At the Molecular Foundry, we have recently developed methods allowing us to fabricate reproducible optical-antenna-based scan probes. These probes provide large near-field enhancements without the constraints of the tip-substrate gap mode.

Our nanoantenna-based tips are fabricated using the induced-deposition mask lithography (IDML) technique (**Figure 2**a–c), the details of which are described in.[81] This method can create high-resolution plasmonic and photonic nanostructures on nearly any substrate, including the apexes of scan-probe tips, with high yields and reproducible performance. An example of a Au bowtie optical antenna on a tip is shown in Figure 2d. The Au nanoantennas are 20-nm thick on top of a 3-nm Ti adhesion layer. Their size and geometry were chosen such that the dipolar plasmon mode would be resonant with a 785-nm excitation laser. TERS experiments were performed by focusing a laser polarized along the bowtie axis through the sample and onto the bowtie tip. The antenna then creates an enhanced, localized optical field near the bowtie gap, where the size of the enhanced field spot is determined primarily by the gap width and the radii of curvature of the antenna tips nearest the gap. Of the many possible nanoantenna geometries, the bowtie antenna was used here due to the relative weakness of the secondary hot-spots that exist at the back sides of the antenna (though, using IDML, most other types of antennas can be fabricated on the tip depending on the specific application[82,86–88]). The TERS signal originating from within the calculated zeptoliter mode volume of the antenna, as well as any background signal excited by the larger but weaker diffraction-limited excitation spot, are collected by the excitation objective, then sent to a spectrometer and charge-coupled device (CCD) camera (Figure 2e experimental schematic).

2.1.1. Evaluating Local Enhancement

The local near-field enhancement factor in a given a-NSOM measurement has proven notoriously difficult to quantify. It is a frequency-dependent quantity, and the square of the field enhancement is often referred to as the intensity enhancement factor. In TERS experiments, the TERS signal should be proportional to the product of the intensity enhancement factor at the excitation frequency and the intensity enhancement factor at the Raman-scattered frequency. Often, it will be said that the TERS signal is proportional to the fourth power of the field enhancement factor (the square of the intensity enhancement factor), but this is not strictly true since the excitation light is at a different wavelength than the outgoing scattered light. Discrepancies between enhancement factor values reported in the literature have been discussed in ref. [35] where the authors note multiple potential sources of variability including differences in tip material, fabrication, and morphology, as well as illumination and detection schemes, nanoscopic sample details, and reflection and confinement of light between the tip and the sample. They suggest a more standardized methodology for estimating enhancement factor using a one-dimensional nanostructure such as a carbon nanotube.

Based on the large number of unknowns involved in calculating an exact enhancement factor, we have chosen in our work presented in this section to evaluate field enhancement using the conservative measure of the "tip-down" vs "tip-up" (TDTU) signal enhancement (e.g., the increase in Raman scattering intensity when the tip is brought close to the sample), which is dependent on tip near-field enhancement, but also on factors such as the size and dimensionality of the sample. This method is possible when a non-background-free illumination scheme is employed, and does not attempt to account for assumed differences between the large sample volume illuminated by the (relatively weak) far-field excitation spot and the nanoscale volume excited by the enhanced near-fields in the vicinity of the tip. It is simply an overall measure of how much the signal changes when a tip is brought near the sample, and is ultimately the factor that directly impacts experimental quantities such as integration times and achievable contrast.

In standard (non-gap-mode) a-NSOM TERS experiments, TDTU values tend to be ≈10, though numbers as large as ≈100 have been reported.[89] In the tip-substrate gap mode, TDTU enhancements exceeding 10^3 have been observed.[72] The primary aim in designing nanoantenna-based probes that effectively put the gap on the tip is to provide similar enhancements to tip-substrate gap mode, but without the limitations of that modality, thereby increasing both the sensitivity and generality of TERS spectroscopy.

2.1.2. TERS on Carbon Nanotubes

To test our probes, we investigated single-walled CNTs grown on a fused silica substrate. CNTs have been investigated extensively via near-field optical spectroscopy and are therefore an ideal test sample.[33,90–92] An atomic force microscope (AFM) image taken in contact mode with a bowtie tip is shown in **Figure 3**. While the rather flat geometry of the probe tips puts constraints on our lateral resolution (see Figure 2d), CNTs and

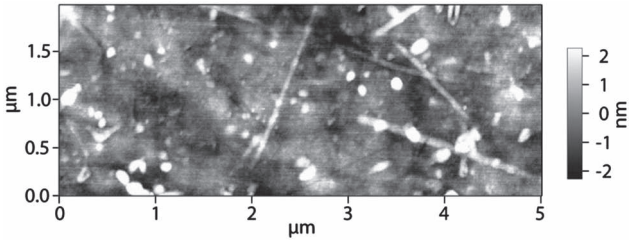

Figure 3. An AFM image of ferrite catalysts and CNTs grown on fused silica, imaged with a bowtie antenna scanning probe.

catalyst particles are easily seen in the AFM scans. We note that the flat bowtie tip apex leads to increased tip-sample interaction relative to a sharp tip, which in some cases resulted in the repositioning or dragging of objects on the sample during AFM scans. This is not an issue when investigating strongly bound samples, such as those described in,[93] but it must be considered when studying softer or more delicate samples. We have also used bowtie tips in tapping mode since the antennas can be fabricated on any type of cantilever. A large tapping-mode oscillation amplitude was required to overcome the substantial tip-sample interaction forces, which significantly reduced the TERS signal due to the small fraction of time the tip, with its localized light spot, spends near the sample surface (i.e. the small duty cycle).

Once a CNT was located, we investigated the TERS characteristics of our bowtie tips by positioning the tip on the CNT, then measuring the TDTU enhancement. An example of our TDTU data is shown in **Figure 4**. With the bowtie tip in contact with the sample, a TERS spectrum was collected using an incident power of 1 µW and a 100 s integration time (Figure 4, blue

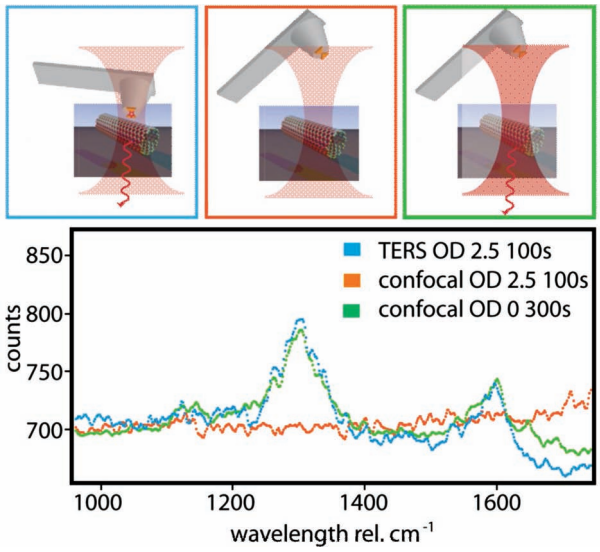

Figure 4. Determining the tip-induced Raman signal enhancement, based on tip-down vs tip-up measurements. With the tip on the sample, 1 µW produced clear D and G mode signal. Using the same power with the tip retracted resulted in no measureable Raman signal. Only after increasing the power 300 times and integration time by a factor of 3, was a comparable Raman signal achieved.

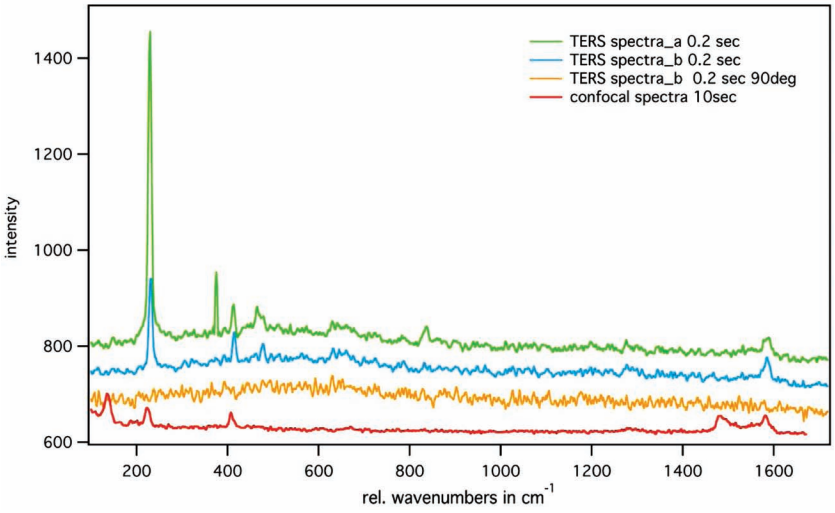

Figure 5. Raman spectra over SWNTs. The green and blue spectra represent TERS spectra at two positions 50 nm apart, but within the same diffraction-limited spot area. The orange spectrum is a TERS spectrum where the polarization of the laser is turned 90 degrees from the main bowtie antenna axis. The red spectrum is the confocal Raman spectrum taken in the same region. Breathing modes between 100 and 300 cm^{-1} can be observed as well as D and G-modes between 1200 and 1600 cm^{-1}. Additionally, intermediate Raman modes can be observed between 350 and 1000 cm^{-1}.

curve). The tip was then retracted approximately 5 μm from the sample and another spectrum was acquired with the same excitation power and integration time. Under these conditions, no significant CNT signal was detected (Figure 4, orange curve). In order to achieve a spectrum comparable to the tip-down case, we had to increase the excitation power by a factor of 300 and integration time by a factor of 3 (Figure 4, green curve), demonstrating at TDTU enhancement of ≈900. Another advantage of these tips is that the enhanced fields are polarized primarily in-plane rather than normal to the surface. In fact, both x- and y-polarization can be equally addressed by fabricating nanoantennas with a cross geometry on the tip. The tips also proved to be rather robust under experimental conditions, with most surviving several hours of contact-mode TERS measurements before changes in tip behavior were observed.

Figure 5 shows four Raman spectra, each vertically offset by 80 counts for clarity. Increasing the laser power to 150 μW produced clear TERS spectra in 0.2 seconds. The green and blue spectra are TERS spectra, labeled a and b, were taken 50 nm apart. The G-mode at 1580 cm^{-1} is visible for both TERS spectra, and the D-mode is less pronounced but can be identified at 1275 cm^{-1}. Differences between the two positions appear in the region between 100 and 600 wavenumbers. Both positions (a) and (b) exhibit a strong Raman peak at 230 cm^{-1}, differing in intensity by a factor of 3. This peak we identified as the breathing mode of a zigzag (13, 0) single wall CNT.[94]

Using TERS, we also find Raman active modes in the spectral region between 350 cm^{-1} and 1000 cm^{-1}. Peaks in this region have been identified as intermediate Raman modes,[95–101] which are typically very weak or absent in conventional Raman spectroscopy of CNTs but enhanced in SERS[102] and TERS measurments.[103] We observe at position (a) (green spectrum) Raman peaks at 375, 413, and 840 cm^{-1}, and a double peak at 463 and 480 cm^{-1}. Position (b) (blue spectrum) features only two peaks in this intermediate region: 413 cm^{-1} and 480 cm^{-1}. The modes in the spectral region between 600 and 1200 cm^{-1} for CNTs have been described as intermediate Raman frequency modes by Dresselhaus et al.[95,96] and Fantini et al.[97,98] The peak we observed at 840 cm^{-1} falls in this intermediate region where Fantini et al. observed a weak but clearly identifiable Raman peak at 860 cm^{-1} in the case of SWNT bundles. The intensity of the intermediate Raman modes measured by Fantini was 30 times weaker than the breathing mode. The intermediate Raman peaks we observe here via TERS show intensities just a factor of 3 less then the breathing modes and comparable to the D-mode. The modes between 600 and 1200 cm^{-1} have been predicted to be active only in very short CNTs, less then 50 nm in length. For longer armchair or zigzag nanotubes only a weak 860 cm^{-1} mode survives.[99,100,104] Mitra et al. simulated Raman modes for finite length CNTs and described the 840 cm^{-1} as a longitudinal mode.[101] Based on this simultaion, the peaks at 375, 413, 463, and 480 cm^{-1} can be interpreted as longitudinal-radial coupled modes. Hence, we are able to strongly enhance both the radial-longitudinal and longitudinal CNT Raman modes using the bowtie antenna tips.

Changing the tip excitation laser polarization 90 degrees at position (b) resulted in a featureless spectrum, also shown in Figure 5, with only the Au photoluminescence background from the antenna still visible. This is consistent with the proper functioning of the antenna: turning the excitation polarization 90 degrees to the bowtie antenna's main axis should reduce the near field enhancement considerably, resulting in little or no observable TERS signal.

To compare TERS data with conventional Raman spectra, a confocal Raman spectrum (red) was collected in the same region using the same polarization as the first two TERS spectra (integration 10 s). The 230 cm^{-1} breathing mode, the 413 cm^{-1} radial-longitudinal mode and the 1580 cm^{-1} G-mode were consistent with TERS. Additionally, the confocal spectrum displays a breathing mode at 176 cm^{-1} and a mode at 1480 cm^{-1}, but is lacking the radial-longitudinal modes at 375, 463, and 480 cm^{-1} and longitudinal mode at 840 cm^{-1}. Since these modes were mainly predicted for finite-length CNTs, we believe that the differences between TERS and confocal Raman signal originate from a combination of mechanical deformation of the CNTs by the tip and differences in near-field vs far-field excitation conditions and selection rules. This phenomena is being investigated further.

2.2. Hyperspectral Nano-Imaging with Coaxial Optical Antenna Scan Probes

The results shown above demonstrate reproducible TERS capabilities for plasmonic-bowtie scan probes, revealing TDTU

enhancements as large as those created in gap-mode TERS—but without the limitations of gap-mode operation. The bowtie-based scan probes also have a downside: namely, the relatively flat structure of the tip apex results in comparatively poor topographic images and large tip-sample interaction forces. This led us to create a new class of probes built on the coaxial (coax) plasmonic antenna concept.[82] A coax aperture can be thought of as a metal-insulator-metal slit or antenna aperture wrapped back onto itself, allowing low-loss polarization-preserving propagation of optical-frequency modes.[105–108] Recent simulations have suggested that the optical coax geometry can be relatively broadband and efficient at coupling to far-field radiation.[105,106,109] By fabricating the center conductor with a tapered end, a coax-based probe combines the advantages of plasmonically-coupled antennae (polarization flexibility; larger fields) with sharp tips, and with the additional option of back-illumination (transmission mode) operation for nearly-background-free imaging.[93,110]

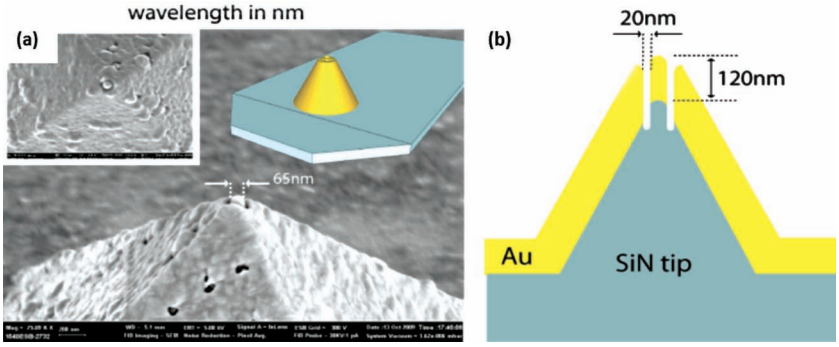

Figure 6. Coaxial optical antennae: A model and an actual coaxial antenna incorporated on the end of a Scanning Probe Tip are shown in (a) and the cross section of the coaxial scan probe is represented in (b). Reproduced with permission.[82] Copyright 2011, American Chemical Society.

Coax tips were fabricated by depositing a 2-nm Ti adhesion layer followed by 120 nm of Au onto commercial (NanoSensors) SiN contact-mode atomic force microscope (AFM) cantilevers. A Focused Ion Beam (FIB) lithography system (Zeiss XB1540) operating at 1-pA beam current and ≈12-nm resolution was used to mill an annular gap around a 65-nm central pin to create the coax structure. To ensure maximum coupling between outer and inner parts of the coaxial structure, we kept the insulating gap constant and as small as possible (15 to 18 nm, i.e., significantly sub-wavelength). It is important to note that the FIB fabrication process induces some curvature and tapering of the central pin (**Figure 6**a), which is desirable for AFM imaging.

The coax probe was fabricated with a 65 nm coax pin diameter, giving it a resonance that matches the 633 nm HeNe laser line used for the Raman imaging experiments. Furthermore, we also demonstrated that the coaxial antennas maintain far-field polarization in transmission. Optical coax properties are strongly dependent on structure. De Waele et al. determined the coaxial waveguide's transmission as a function of the length and gap of the coaxial structure,[109,111] showing super-enhanced resonant transmission. Others have simulated coaxial openings for a variety of film thicknesses and determined the dependence on inner pin diameter in the visible regime for perfect electrical conductor (PEC) thicknesses on the order of 100 nm.[105]

It is important to note that linearly polarized light excites the first order mode for a symmetric coax with a perfectly cylindrical center pin (flat top and bottom surfaces), as the lowest order mode is not dipole active due to symmetry. This is expected to create two localized hot spots at the end of the coax along the polarization direction.[106,109] The lowest order mode could alternatively be excited by radially polarized or z-polarized light. We have attempted to create a more singular primary localized field volume by tapering[22] and rounding the ends of our coax center pins, which also aids AFM imaging performance. In practice, our Raman images are consistent with a single (vs double) near-field spot signature as shown below. This may result from one hot spot being closer to the sample when the AFM tip contacts the surface, or to eccentricity or asymmetry in the coax structure resulting from the nanofabrication process, leading to one dominant hot spot.

The coax tips were excited through the fused silica substrate using a linearly-polarized HeNe laser focused by a 100× 1.4NA oil objective. The scattered Raman light was collected through the same objective and directed onto either a grating spectrometer with a thermoelectrically-cooled CCD camera or a photo multiplier tube (PMT) using a dichroic mirror and long-pass filter. The dichroic rejected scattered light within 400 cm^{-1} of the laser line, preventing the observation of the carbon nanotube (CNT) radial breathing modes. To obtain a near-field signal, the laser (100 μW) was focused on the sample surface, then the tip was moved into the laser focus. The signal was optimized by scanning the laser over the tip apex with a 2D galvanometer (Thorlabs) while recording the Au photoluminescence (PL) signal on the PMT, then placing the laser focus at the position of maximum PL.

We demonstrated the spectroscopic imaging capabilities of our coaxial tips by imaging carbon nanotubes that were grown directly on fused silica cover slips. **Figure 7**a shows a topographic AFM scan acquired with a coax antenna probe. The lateral resolution is on the order of 20 nm, consistent with the radius of curvature of the central coax pin and the coax gap size. Based on several line scans over the sample, many of the CNT structures appear to be either multiwall CNTs or single wall CNT bundles.

The sample was then positioned so that the tip was placed on a CNT (marker in Figure 7a) and the Raman spectrum was recorded (Figure 7b). The 10-s-long spectrum clearly shows the D and G modes at 1308 and 1586 wave numbers along with a PL background originating from the Au antenna. The D- to G-mode intensity ratio was ≈4.5. The AFM tip was then retracted to take a far-field confocal spectrum (Figure 7c) of the same area. The spectrum was integrated 12 times longer to achieve a comparable G-mode signal. In confocal mode, the D/G mode ratio was ≈1. The increase in the D/G mode ratio for the tip-enhanced spectrum could be caused by localized strain on the CNT induced by the tip in contact mode. Yano et al. observed an intensity increase and position shift of the G-mode

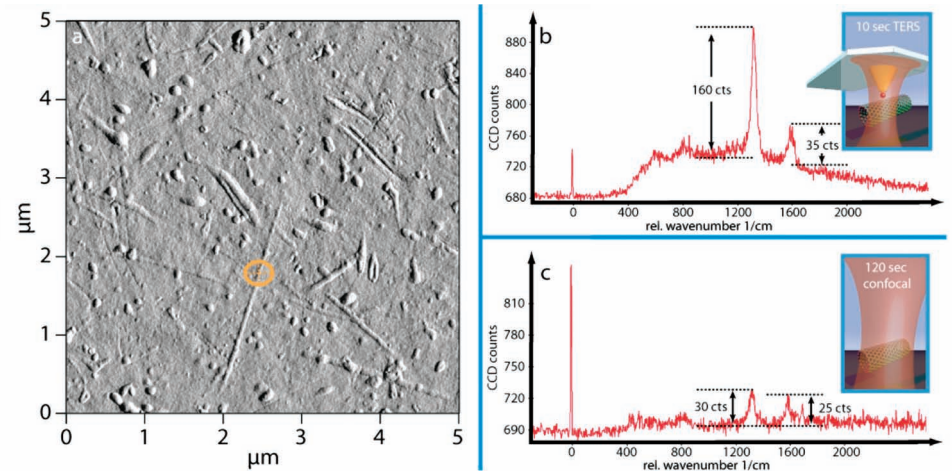

Figure 7. Tip Enhanced Raman Spectroscopy on CNTs using a coax probe. a) Topographic error-signal image of CNTs grown on a fused silica cover slip acquired with the coaxial antenna scanning probe. b) Tip-enhanced Raman spectrum of the CNT taken at the marked position in a), integrated over 10 s. c) confocal Raman spectrum at the equivalent position. An integration time of 120 s was necessary to achieve a similar G-mode signal. Reproduced with permission.[82] Copyright 2011, American Chemical Society.

when applying pressure using a sharp metal tip as their near-field probe.[33] In contrast we observed variations in the D-mode intensity and no detectable peak shifts. We tested various tips and exerted different tip forces on the sample but the intensity of the G-mode was not affected within our experimental resolution. This discrepancy may be related to the different polarizations of the excitation light for the two types of tips (mostly in-plane vs z-polarized), though further studies are required for better understanding.

Due to the load-dependent D-mode intensity variations, we choose to use the G-mode intensity to compare tip-enhanced and confocal Raman intensity. The data shown here give a TDTU G-mode enhancement of 17 (D-mode enhancement of 64). We stress that the nanofabricated tip yield approaches 100%—all of the tips that look good in post-FIB SEM images demonstrated significant Raman enhancement. The coax tips were also sufficiently durable to support many hours of contact-mode imaging.

Increasing the focused laser power to 150 µW led to satisfactory signal-to-noise ratios in the Raman spectra for integration times as low as 50 ms, enabling practical *hyperspectral* Raman mapping on dielectric substrates–i.e. we were able to take a full Raman Spectrum at each pixel of a near-field imaging scan. While performing a slow 1.5 µm by 1.5 µm AFM scan over our sample (see **Figure 8**a topography image), spectra were acquired at each of the 256 by 256 pixels, allowing the detection of small variations in the sample chemistry and composition, reflected by small changes in peak positions and intensities. A typical 0.1 s spectrum over the CNTs is shown in Figure 8b.

Spectral maps were generated by subtracting the PL background and integrating the Raman peaks from 1250 to 1350 cm^{-1} for the D-band (see Figure 8c) and from 1550 to 1650 cm^{-1} for the G-band (see Figure 8d). The D-mode map, related to the CNT defect density, shows rich detail and strong

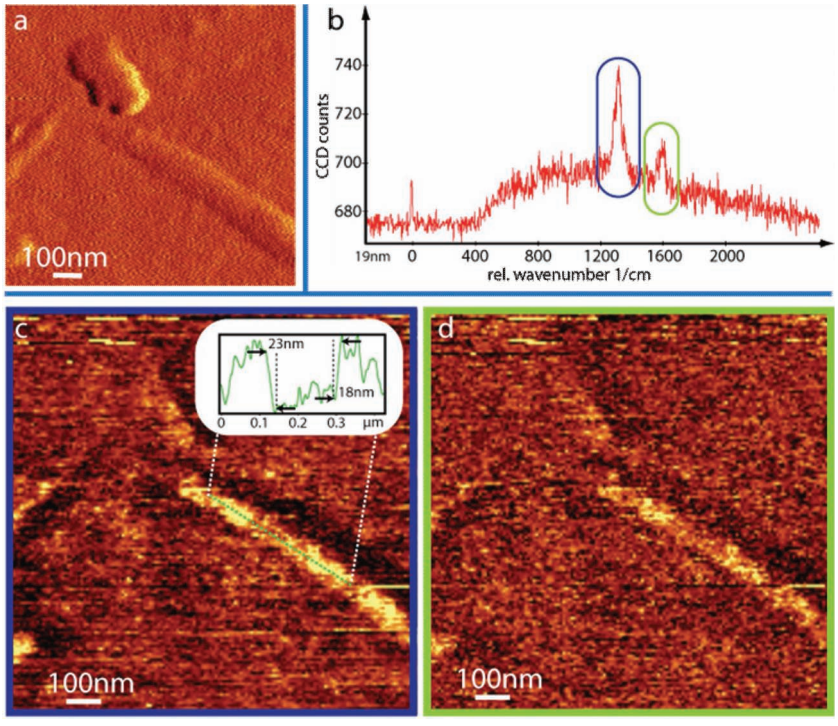

Figure 8. Raman spectral mapping of CNTs. a) topography of mapped region (error signal). b) example of 0.1 s Raman spectrum which was taken at each pixel. D and G peaks are shown with a blue and green circle, respectively. c,d) Corresponding intensity maps of the D and G peaks. The inset in (c) is a line-scan demonstrating the optical resolution along the CNT structure. We additionally observed polarization dependence for the imaging performance, which we will report on in a following publication. Reproduced with permission.[82] Copyright 2011, American Chemical Society.

local variation in intensity, in principle enabling us to map CNT defects with a resolution below 20 nm. These variations do not originate from topographic effects since the height over the CNT structure was fairly constant. In this particular case, we also observed G-band intensity variations due to the presence of a bundle of SWCNTs.

Lateral optical resolution was determined from a line scan of the D-mode intensity variation along the top of a CNT structure (inset Figure 8c). This approach avoids optical artifacts arising from convolution of optical response with the sample topography. There were no significant changes in CNT topography along this line, demonstrating that the observed optical signal changes arise from the intrinsic properties of the sample. Here, the D-mode line-scan shows a sharp decrease as well as an increase (inset Figure 8c) with transition widths of 23 and 18 nm, respectively, leading us to estimate a lateral optical resolution ≤23 nm. Line scans over apparent catalyst particles that showed a D-mode signal due to initial growth of CNTs had an optical width of around 22 nm, comparable to the line scan along the CNT.

These results show that the coax probe geometry combines the spectroscopic advantages of coupled resonant optical antennas with the good AFM imaging properties of sharp tips. In fact, they were the first demonstration of hyperspectral nanoimaging in the *non*-tip-substrate gap mode–an important step towards the generalized use of nano-optics in the study of materials.[82] But similar to other resonant antenna tips, these truncated coaxial plasmonic probes still possess limitations, which we have recently been able to address.

2.3. Pushing Towards the Ideal Nano-Optical Probe: Hyperspectral Nanoimaging with "Campanile" Tips

The advanced probes described above greatly increase both the sensitivity and generality of TERS imaging and spectroscopy. However, because of their antenna designs, such probe geometries have relied on resonant structures and excitation modes that are not background-free, i.e., the excitation beam illuminates at least a diffraction-limited region on the sample along with the plasmonic tip structure. In these cases, excitation can be through the (transparent) sample substrate or from the side. This results in a competition between the enhanced signal originating from within the zeptoliter mode volume of the optical antenna, and background photons from the more weakly-excited but much larger illumination spot.[35] It is worth noting that background signal depends on the dimensionality of the sample; point, line, or surface Raman-active samples have better ratios of enhanced signal to unenhanced background than do bulk samples.[35]

Illumination of the sample outside the nano-region of interest has been recognized as a significant problem by the nano-optics community. Therefore, a number of next-generation near-field tip geometries based on extraordinary optical transmission (EOT) structures - and the related plasmonic antenna apertures - have been realized.[112–115] Here, light incident on the back of the structure is transmitted through a nanoscale aperture with much higher efficiency than that achieved by conventional aperture-based probes, illuminating only the nanoscale volume of interest. However, while transmission efficiency is high, overall field enhancement is generally lower than what has been realized by the plasmonically-coupled antenna probes described above. And perhaps just as importantly, both plasmonically-coupled antenna (e.g., bowtie) probes and EOT-type probes are, by design, resonant structures. As mentioned above, enhancement would ideally be large over a wide spectral range for optimized nanoscale spectroscopic measurements.

The desire to achieve large, broadband near-field enhancement while operating in a background-free excitation mode has led researchers to adopt novel nanofocusing strategies based on the broadband adiabatic propagation and compression of SPP modes on a conically tapered tip. These strategies combine elements of the previously-mentioned a-NSOM tips, which also utilized an adiabatic taper for near-field enhancement, with efficient photon-to-plasmon coupling structures that can be illuminated far from the sample, launching a plasmon wave towards the tip apex and avoiding most unwanted background excitation. For example, grating couplers were fabricated a few microns up the conical adiabatic taper (CAT) tip shaft,[110,116,117] leading to far-field to near-field coupling efficiencies of ≈2–4%. Though grating couplers are narrow-band by design, Raschke and coworkers have cleverly "chirped" the grating spacing within the far-field illumination area to enable SPP coupling over a relatively broad wavelength range. Another example is the probe geometry described in,[93] where a photonic crystal fabricated on a cantilever is used to capture and convert light to plasmons propagating adiabatically along a sharp cone located at the center of the photonic crystal cavity. Of course, these photonic crystals are also narrowband couplers, but it is conceivable that more complex designs (e.g., fractal-based structures) could allow for excitation coupling at many wavelengths. Also promising are geometries based on novel ultrasmooth and sharp cone and pyramid tips.[83,84,118,119]

These types of probes represent a significant step forward, as they efficiently integrate the advantages of broadband photon-to-plasmon couplers, plasmonic waveguides, and optical antennas. They have recently demonstrated large TERS enhancements from a number of different samples including single molecules and silicon nanocrystals. However, there is one primary drawback to these CAT tips: maximum enhancement is still only achieved in the tip-substrate gap mode. Thus, the question remains: is it possible to realize the best properties of these CAT tips in a structure that moves beyond this limitation?

We have recently demonstrated a revolutionary tip concept based on a unique geometry capable of efficiently coupling far-field light to the near-field and *vice-versa* without background illumination, and more significantly, doing so over a wide range of wavelengths.[120] The probe geometry is based on a 3D tapered metal-insulator-metal (MIM) structure ending in a nanogap (**Figure 9**a–c), with a shape resembling that of the "campanile" bell tower of Venice, which is reproduced at the Berkeley campus (hereafter referred to as campanile). Our simulations show that this geometry provides efficient coupling between far- and near-fields (Figure 9d) since the fundamental mode in the MIM structure is supported without any cut-off frequency no matter how thin the insulating layer.[121]

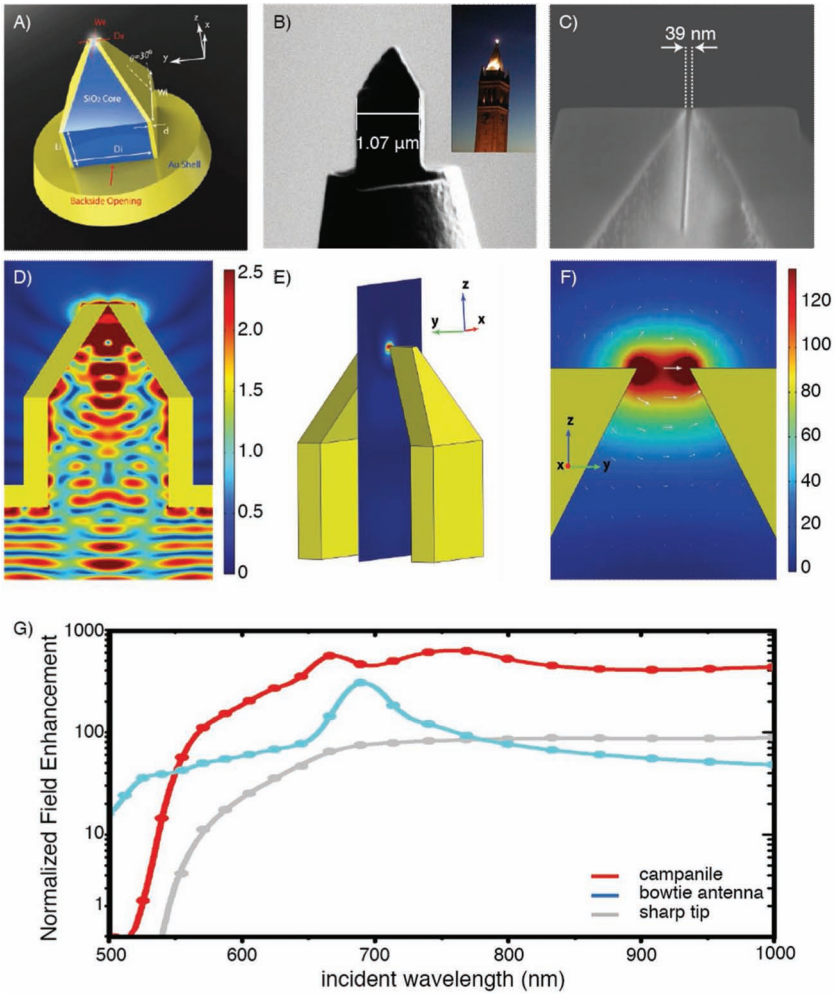

Figure 9. Structure and optical properties of the 3D-tapered (campanile) far-field to near-field transformer. The campanile geometry (A) is comprised of a tapered metal-insulator-metal waveguide fabricated at the end of a tapered glass fiber (B) by focused ion beam milling. Its shape resembles a bell tower of the same name (inset: photo of the Berkeley campanile), with a 39 nm (±2 nm) gap between the 3D-tapered Au plates (C). D) Finite Element simulations reveal the highly efficient bi-directional coupling between macro and nanometer length scales (the color-scale contrast of electric field strength is saturated to show the much weaker photonic and weakly-confined plasmonic modes). Extending the contrast over the full color scale shows the nearly-background-free near-field enhancement at the tip apex (E) while maintaining the linear polarization of the far field (F) (gap size = 10 nm; λ = 667 nm). (G) The ultra-large field enhancement for a campanile with a 2-nm gap extends over an enormous band-width (red curve) compared to a coupled optical bowtie antenna (blue curve) with a 2 nm gap or a sharp Au tip with a 20-nm radius of curvature (grey curve; assuming 100% light-coupling efficiency to the Au tip). The campanile structure, with its broadband field enhancement and highly efficient, nearly-background-free bi-directional coupling between far- and near-fields, is ideal to bring optical techniques to the nanoscale. Reproduced with permission.[120] Copyright 2012, American Association for the Advancement of Science.

In the optical regime, where plasmonic effects become important at small length scales, it has been shown that efficient delivery of far-field light to an ultra-small region is possible in two dimensions using a tapered planar MIM structure (>70% conversion efficiency),[122–124] and in three dimensions with a dimple lens structure.[125] Equally important, the bi-directional coupling of the campanile probe is efficient over a large band-width (Figure 9g), similar to the adiabatically-tapered[22,121] geometries utilized in the microwave and terahertz regimes.[126] This is one of the simplest broadband methods for effectively overcoming the diffraction limit. The bandwidth is limited only by metal absorption at short wavelengths, and can be extended well into the infrared region. Other metals can be used to access the blue or ultraviolet (UV) regions. The plasmonic mode in the campanile is adiabatically squeezed into the nanogap region. Therefore, as shown in Figure 9e–f, the size of the campanile gap primarily defines the spatial resolution as well as the field enhancement, which is greater than that from a bowtie antenna with the same size gap (Figure 9g).

Figure 9e shows that the campanile operation is also nearly-background-free. Within the taper region, only a few photons escape due to edge scattering and leakage before reaching the tip apex. We operate the campanile probe in a mode where signal is collected back through the nanogap, so the collected background from the sample arising from the edge-scattered light is expected to be insignificant and was below the noise threshold in the PL images shown here. In addition, as with all near-field probes, the campanile tips interrogate only surface/interface material located within a few nm of the tip apex (Figure 9f), eliminating most background spectroscopic signal arising from bulk material or surrounding fluid.

Using standard nanofabrication techniques, the campanile design can be integrated into the apex of a number of scan probes including atomic force microscope (AFM) cantilevers and tapered optical fibers such as those used in conventional aperture-based NSOM. Representative images of a campanile tip are shown in Figure 9b,c. For a linearly tapered 3D MIM structure, the optimal taper angle is around 20°–40°, over which range the transfer efficiency shows only minor changes.[121] Note that since a tapered coaxial structure is a cylindrical analog to the MIM, it should have similar properties to the campanile.

Before discussing the experimental results from the campanile tips, a couple comments on coupling efficiency and loss are in order, particularly in relation to CAT tips. In terms of coupling far-field excitation light to plasmon modes on a tip (and vice versa), extremely high coupling efficiencies are possible (≈95–100% in the visible and IR) if the transducer is optimized for operating at a specific wavelength rather than over a broad spectrum. This is achieved by engineering geometric resonances into the tip design, both for CAT tips and campanile structures.[127] Such high efficiencies are important for single-photon and

related quantum optics applications. For broadband coupling, efficiencies appear to be somewhat lower, likely approaching ≈70%.[122,127] However, for campanile-type structures, 3D broadband designs are still being optimized, making this a current area of study.

From an energy loss point of view, both the campanile and CAT tips can perform well, where the limitations are primarily propagation loss and radiation.[121,127] That said, there may be some practical/technical advantages for using a 3D tapered-MIM geometry like the campanile or a coaxial structure. For one, CAT tips require a coupler of some sort for converting photonic modes to plasmonic modes, whereas the tapered MIM itself acts both as the coupler and, further down the adiabatic taper, as the mode compressor. Also, plasmon propagation occurs along the relatively smooth metal-dielectric surfaces of the tapered MIM structures, whereas plasmons travel along the outer surface of the CAT tips, which is often more rough (when fabricated using chemical etching or standard metal deposition techniques), resulting in more scattering and radiation. This problem, though, has been recently addressed using template-stripping methods for creating CAT and other similar probe tips.[84] In addition, there may also be some advantages to operating in a MIM geometry vs the IMI geometry of the CAT tip in terms of mode propagation distances within the taper, though this is difficult to say without further study.

To demonstrate the utility of the tapered-MIM probe concept, campanile tips with ≈40 nm-wide apertures were used to map out the inhomogeneous radiative recombination in individual InP NWs, chosen because of their PL emission properties and their potential for light harvesting due to their 1.4 eV bandgap and assumed low surface recombination rates.[128–130] Trap states are believed to be responsible for many optical phenomena in nanocrystals and wires,[131,132] including surface-state-mediated luminescence modification in InP NWs,[133] but are not well-understood due to difficulty of doing optical measurements at the relevant length scales. We gain crucial insights into nanostructure properties by performing both local optical excitation *and* local luminescence collection.

The glass fiber with the campanile tip was mounted in a shear-force scanner and coupled to a 633 nm laser. The near-field spot was scanned over the sample to locally excite and collect the PL from the InP NWs. Because of the huge broadband enhancement, only 100 μW of pre-fiber-coupled laser excitation power (<1/10th of a basic laser pointer) was needed to acquire a full emission spectrum in 100 ms with a signal-to-noise ratio > 60:1.

A full spectrum was recorded at each topography image pixel, and PL maps were built by taking slices from the hyperspectral data. **Figure 10** shows a 95-nm-wide InP NW imaged with a scanning electron microscope (SEM) (Figure 10a), the campanile tip (Figure 10b), and a far-field confocal microscope (Figure 10c). The confocal excitation power was equivalent to that used for the campanile tip and achieved a comparable signal to noise ratio. The campanile tip clearly provides resolution approximately equal to the gap size and much higher than the confocal resolution (Figure 10d) (see linescan in Figure 10e, taken along the smooth NW in order to rule out topographical artifacts in our estimate of measured resolution).

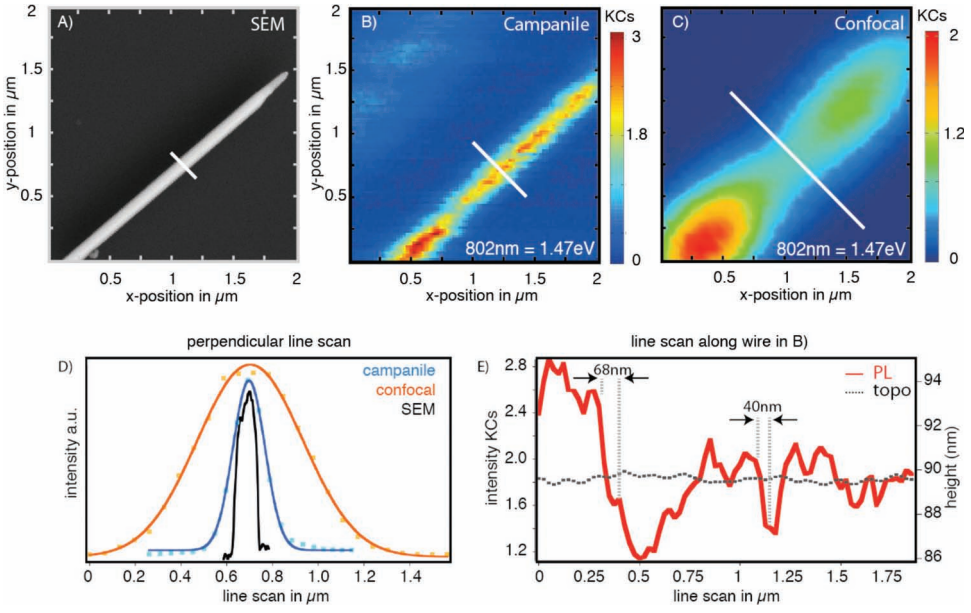

Figure 10. Nano-optical hyperspectral photoluminescence mapping of InP nanowires. A) SEM image of an InP NW that was hyperspectrally mapped B) with the campanile tip (100 μW excitation power, 100 msec/spectrum, map at 802 nm), and C) confocally (900 μW, 10 msec/spectrum, map at 802 nm). The near-field map (B) has considerably higher spatial resolution then the confocal map, as shown by line scans across the wire (D), and strong local PL variations along the wire. E) A line scan along the wire in (B) reveals a spatial resolution of ≈40 nm (approximately equal to the gap size) while the same line scan along the topography image shows no variation. Reproduced with permission.[120] Copyright 2012, American Association for the Advancement of Science.

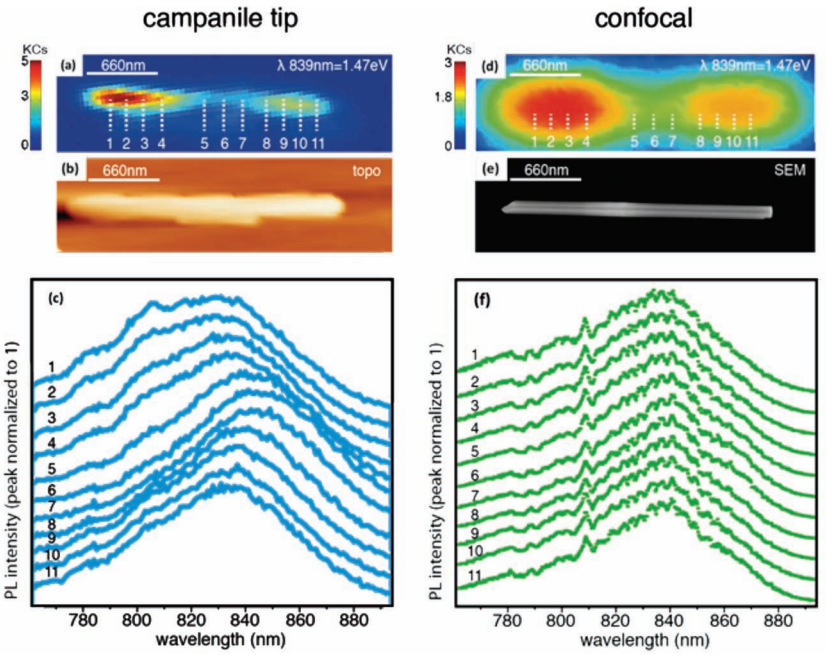

Figure 11. a) InP NWs displayed one or two PL intensity hot spots typically 250–300 nm from the wire ends compared to b) topography and e) SEM images of the same NW. A waterfall plot of near-field spectra taken at the positions 1–11 (emission intensity normalized to one) shows strong local spectral variations, with the PL hot spots showing a band edge blue shift as well as stronger contributions from trap-related above-bandgap spectral components (c). In contrast, the same wire imaged confocally (d) also displays two maxima but no spectral variations along the NW (f). Reproduced with permission.[120] Copyright 2012, American Association for the Advancement of Science.

PL spectra acquired using the campanile tip and a far-field confocal microscope can be seen in **Figure 11**. The band edge emission peak at 889 nm (1.47 eV), corresponds to the expected 100 meV blue shift relative to bulk InP NWs, independent of quantum confinement.[133] Moreover, we observe various shoulders 40-100 meV above the band edge emission that broaden the spectra considerably. With the campanile tip, we now directly observe spectral intensity and linewidth variations along individual NWs. In addition, for some of the studied wires we observed PL hotspots located approximately 250 to 300 nm from one or both of the wire ends (compare Figure 11a,b). The PL hotspots correspond to a spectral broadening toward the blue associated with additional luminescence contributions from 40–100 meV above the band edge, as seen in the waterfall plot of PL spectra from various points along the wire (Figure 11c; PL peak intensity normalized to one for clarity). In contrast, confocal PL measurements of the same wire (Figure 11d) also displayed two maxima, but could not resolve spectral variations along the NW (Figure 11f) in agreement with previous confocal studies. In other words, with the campanile probe we gain access to a new level of information. In this case, we reveal photoluminescence (PL) heterogeneity along individual nanowires by mapping local charge recombination originating from trap states–critical optoelectronic information unobtainable using previous methods.

We emphasize that the increased density of optical states at the tip apex will change the balance between various recombination pathways and may enable otherwise dark states to radiatively recombine.[24,134,135] We also note that measurements on these NWs (and any sample thicker than ≈2 nm) are not possible with a-NSOM in tip-substrate gap mode. No other near-field/tip-enhanced techniques demonstrated to date have the resolution and sensitivity shown here, which is critical for investigating most nanoscale samples. Based on these results, the campanile geometry appears to be quite promising for future near-field studies, though more direct experimental comparisons between the campanile and other tips are ultimately required before quantitative statements can be made about the potential advantages. These studies are currently underway in our lab.

3. Conclusions and Outlook

Carrying out local optical spectroscopy at the nanoscale is an ongoing challenge for nanoscience. On a fundamental level, this should be possible by squeezing light beyond the diffraction limit. Various optical-antenna-based scan-probe geometries had been designed to address this 'nanospectroscopy imaging' challenge by transforming light from the far-field to the near-field, but unfortunately with serious limitations on sensitivity, bandwidth, resolution, and/or sample types. Significant efforts have been made in the design, fabrication, and implementation of more advanced near-field probes to address these limitations. In our case, the unique collaborative environment at the Molecular Foundry, a Department of Energy (DOE) Nanoscale Science Research Center (NSRC), has resulted in the development of a set of probes that offer novel solutions to the nanospectroscopy imaging problem and constitute new paradigms in plasmonics, non-linear optics, and especially near-field investigations. In addition, as a DOE User Facility, the new nano-optical capabilities at the Foundry enabled by these new tools are now accessible to the larger scientific community, with current users already investigating a wide range of materials including graphene, battery interfaces, and DNA.

Since these innovations are rather recent, it is also worth remembering that there is still much work to be done. For example, realizing the full potential of these probes will require advances in reproducible mass-fabrication of tips; fast and robust chemometric data analysis; in-situ scanning capabilities and tip properties amenable to in-situ studies; and better scan algorithms for fast, efficient multidimensional imaging at multiple length scales. And of course pushing optical studies to the near-atomic regime will require an increase in spatial resolution. Already, the work reported here demonstrates the impact of these novel geometries (particularly the campanile geometry) on a wide range of nano-optical measurements, since virtually all possible categories of optical imaging and spectroscopy can now be brought to the nanoscale, including Raman and IR/FTIR hyperspectral imaging, as well as white-light

nanoellipsometry and interferometric mapping of dielectric functions. Additionally, the combination of large bandwidth and enhancement make them ideal for ultrafast, pump-probe and/or nonlinear experiments down to molecular length scales, where they would be used for ultrasensitive medical detection, (photo)catalysis and quantum-optics investigations, as plasmonic optomechanics and circuitry elements, and as the cornerstone of tabletop high-harmonic/X-ray and photoemission sources. In short, these new scan-probe tools and techniques provide access to a new world of physics and dynamics within materials that has yet to be studied.

Acknowledgements

The authors specifically thank Ed Wong for fast and high-quality technical support, as well as our colleagues at the Molecular Foundry for stimulating discussion and assistance. We specifically thank W. Bao, M. Melli, F. Intonti, D. S. Wiersma, Y. D. Suh, O. Yaghi, S. Aloni, J. B. Neaton, E. Yablonovitch, J. Bokor, and M. B. Salmeron for their valuable contributions to this effort. Work at the Molecular Foundry was supported by the Director, Office of Science, Office of Basic Energy Sciences, Division of Materials Sciences and Engineering, of the U.S. Department of Energy under Contract No. DE-AC02-05CH11231.

Received: November 21, 2012
Published online: March 26, 2013

[1] L. Novotny, B. Hecht, *Principles of Nano-Optics*, Cambridge University Press, Cambridge, UK **2006**.
[2] D. A. Bonnell, D. N. Basov, M. Bode, U. Diebold, S. V. Kalinin, V. Madhavan, L. Novotny, M. Salmeron, U. D. Schwarz, P. S. Weiss, *Rev. Mod. Phys.* **2012**, *84*, 1343.
[3] E. Betzig, G. H. Patterson, R. Sougrat, O. W. Lindwasser, S. Olenych, J. S. Bonifacino, M. W. Davidson, J. Lippincott-Schwartz, H. F. Hess, *Science* **2006**, *313*, 1642.
[4] S. T. Hess, T. P. K. Girirajan, M. D. Mason, *Biophys. J.* **2006**, *91*, 4258.
[5] V. Westphal, S. O. Rizzoli, M. A. Lauterbach, D. Kamin, R. Jahn, S. W. Hell, *Science* **2008**, *320*, 246.
[6] W. E. Moerner, *Proc. Natl. Acad. Sci. USA* **2007**, *104*, 12596.
[7] M. A. Paesler, P. J. Moyer, *Near-field optics: theory, instrumentation, and applications*, Wiley, New York **1996**.
[8] E. H. Synge, *Philos. Mag.* **1928**, *6*, 356.
[9] D. W. Pohl, W. Denk, M. Lanz, *Appl. Phys. Lett.* **1984**, *44*, 651.
[10] A. Lewis, M. Isaacson, A. Harootunian, A. Muray, *Ultramicroscopy* **1984**, *13*, 227.
[11] E. Betzig, R. J. Chichester, *Science* **1993**, *262*, 1422.
[12] E. Betzig, J. K. Trautman, *Science* **1992**, *257*, 189.
[13] L. Novotny, C. Hafner, *Phys. Rev. E* **1994**, *50*, 4094.
[14] H. A. Bethe, *Phys. Rev.* **1944**, *66*, 163.
[15] J. Gersten, A. Nitzan, *J. Chem. Phys.* **1980**, *73*, 3023.
[16] J. Jackson, *Classical Electrodynamics Third Edition*, Wiley, New York **1998**.
[17] S. Kawata, Y. Inouye, P. Verma, *Nat. Photonics* **2009**, *3*, 388.
[18] A. J. Babadjanyan, N. L. Margaryan, K. V. Nerkararyan, *J. Appl. Phys.* **2000**, *87*, 3785.
[19] K. V. Nerkararyan, *Phys. Lett. A* **1997**, *237*, 103.
[20] K. Nerkararyan, T. Abrahamyan, E. Janunts, R. Khachatryan, S. Harutyunyan, *Phys. Lett. A* **2006**, *350*, 147.
[21] M. I. Stockman, S. V. Faleev, D. J. Bergman, *Phys. Rev. Lett.* **2001**, *87*, 167401.
[22] M. I. Stockman, *Phys. Rev. Lett.* **2004**, *93*, 137404.
[23] P. Anger, P. Bharadwaj, L. Novotny, *Phys. Rev. Lett.* **2006**, *96*, 113002.
[24] S. Kuhn, U. Hkanson, L. Rogobete, V. Sandoghdar, *Phys. Rev. Lett.* **2006**, *97*, 017402.
[25] J. M. Gerton, L. A. Wade, G. A. Lessard, Z. Ma, S. R. Quake, *Phys. Rev. Lett.* **2004**, *93*, 180801.
[26] E. J. Sanchez, L. Novotny, X. S. Xie, *Phys. Rev. Lett.* **1999**, *82*, 4014.
[27] N. Hayazawa, Y. Inouye, Z. Sekkat, S. Kawata, *Opt. Commun.* **2000**, *183*, 333.
[28] R. M. Stockle, Y. D. Suh, V. Deckert, R. Zenobi, *Chem. Phys. Lett.* **2000**, *318*, 131.
[29] M. S. Anderson, *Appl. Phys. Lett.* **2000**, *76*, 3130.
[30] T. Ichimura, N. Hayazawa, M. Hashimoto, Y. Inouye, S. Kawata, *Phys. Rev. Lett.* **2004**, *92*, 220801.
[31] Y. Ogawa, T. Toizumi, F. Minami, A. V. Baranov, *Phys. Rev. B* **2011**, *83*, 081302.
[32] N. Hayazawa, M. Motohashi, Y. Saito, S. Kawata, *Appl. Phys. Lett.* **2005**, *86*.
[33] T. Yano, P. Verma, Y. Saito, T. Ichimura, S. Kawata, *Nat. Photonics* **2009**, *3*, 473.
[34] S. Berweger, C. C. Neacsu, Y. B. Mao, H. J. Zhou, S. S. Wong, M. B. Raschke, *Nat. Nanotechnol.* **2009**, *4*, 496.
[35] D. Roy, J. Wang, C. Williams, *J. Appl. Phys.* **2009**, *105*, 013530.
[36] J. Wessel, *J. Opt. Soc. Am. B* **1985**, *2*, 1538.
[37] Y. Inouye, N. Hayazawa, Z. Sekkat, S. Kawata, *Abstr. Pap. Am. Chem. Soc.* **2001**, *221*, U95.
[38] F. Zenhausern, M. P. Oboyle, H. K. Wickramasinghe, *Appl. Phys. Lett.* **1994**, *65*, 1623.
[39] R. Bachelot, P. Gleyzes, A. C. Boccara, *Microsc. Microanal. Microstruct.* **1994**, *5*, 389.
[40] B. Knoll, F. Keilmann, *Nature* **1999**, *399*, 134.
[41] L. Novotny, S. J. Stranick, *Annu. Rev. Phys. Chem.* **2006**, *57*, 303.
[42] L. Gomez, R. Bachelot, A. Bouhelier, G. P. Wiederrecht, S. H. Chang, S. K. Gray, F. Hua, S. Jeon, J. A. Rogers, M. E. Castro, S. Blaize, I. Stefanon, G. Lerondel, P. Royer, *J. Opt. Soc. Am. B* **2006**, *23*, 823.
[43] T. Taubner, R. Hillenbrand, F. Keilmann, *J. Microsc.* **2003**, *210*, 311.
[44] R. Esteban, R. Vogelgesang, K. Kern, *Ultramicroscopy* **2011**, *111*, 1469.
[45] R. L. Olmon, P. M. Krenz, A. C. Jones, G. D. Boreman, M. B. Raschke, *Opt. Express* **2008**, *16*, 20295.
[46] R. L. Olmon, M. Rang, P. M. Krenz, B. A. Lail, L. V. Saraf, G. D. Boreman, M. B. Raschke, *Phys. Rev. Lett.* **2010**, *105*, 167403.
[47] M. Schnell, P. Alonso-Gonzalez, L. Arzubiaga, F. Casanova, L. E. Hueso, A. Chuvilin, R. Hillenbrand, *Nat. Photonics* **2011**, *5*, 283.
[48] M. Schnell, A. Garcia-Etxarri, A. J. Huber, K. Crozier, J. Aizpurua, R. Hillenbrand, *Nat. Photonics* **2009**, *3*, 287.
[49] D. S. Kim, J. Heo, S. H. Ahn, S. W. Han, W. S. Yun, Z. H. Kim, *Nano Lett.* **2009**, *9*, 3619.
[50] S. Mastel, S. E. Grefe, G. B. Cross, A. Taber, S. Dhuey, S. Cabrini, P. J. Schuck, Y. Abate, *Appl. Phys. Lett.* **2012**, *101*, 131102.
[51] Z. Fei, A. S. Rodin, G. O. Andreev, W. Bao, A. S. McLeod, M. Wagner, L. M. Zhang, Z. Zhao, M. Thiemens, G. Dominguez, M. M. Fogler, A. H. C. Neto, C. N. Lau, F. Keilmann, D. N. Basov, *Nature* **2012**, *487*, 82.
[52] J. N. Chen, M. Badioli, P. Alonso-Gonzalez, S. Thongrattanasiri, F. Huth, J. Osmond, M. Spasenovic, A. Centeno, A. Pesquera, P. Godignon, A. Z. Elorza, N. Camara, F. J. G. de Abajo, R. Hillenbrand, F. H. L. Koppens, *Nature* **2012**, *487*, 77.
[53] J. Dorfmuller, R. Vogelgesang, W. Khunsin, C. Rockstuhl, C. Etrich, K. Kern, *Nano Lett.* **2010**, *10*, 3596.
[54] R. Hillenbrand, T. Taubner, F. Keilmann, *Nature* **2002**, *418*, 159.
[55] M. Brehm, T. Taubner, R. Hillenbrand, F. Keilmann, *Nano Lett.* **2006**, *6*, 1307.

[56] M. M. Qazilbash, M. Brehm, B.-G. Chae, P.-C. Ho, G. O. Andreev, B.-J. Kim, S. J. Yun, A. V. Balatsky, M. B. Maple, F. Keilmann, H.-T. Kim, D. N. Basov, *Science* **2007**, *318*, 1750.
[57] J. M. Stiegler, Y. Abate, A. Cvitkovic, Y. E. Romanyuk, A. J. Huber, S. R. Leone, R. Hillenbrand, *ACS Nano* **2011**, *5*, 6494.
[58] F. Huth, A. Govyadinov, S. Amarie, W. Nuansing, F. Keilmann, R. Hilenbrand, *Nano Lett.* **2012**, *12*, 3973.
[59] J. Stadler, T. Schmid, R. Zenobi, *Nanoscale* **2012**, *4*, 1856.
[60] S. M. Nie, S. R. Emery, *Science* **1997**, *275*, 1102.
[61] A. Jamshidi, S. L. Neale, K. Yu, P. J. Pauzauskie, P. J. Schuck, J. K. Valley, H. Y. Hsu, A. T. Ohta, M. C. Wu, *Nano Lett.* **2009**, *9*, 2921.
[62] A. T. Zayak, Y. S. Hu, H. Choo, J. Bokor, S. Cabrini, P. J. Schuck, J. B. Neaton, *Phys. Rev. Lett.* **2011**, *106*, 083003.
[63] C. F. Bohren, D. R. Huffman, *Absorption and Scattering of Light by Small Particles*, Wiley-VCH Verlag GmbH, Weinheim **2007** .
[64] A. T. Zayak, H. Choo, Y. S. Hu, D. J. Gargas, S. Cabrini, J. Bokor, P. J. Schuck, J. B. Neaton, *J. Phys. Chem. Lett.* **2012**, *3*, 1357.
[65] T. J. Seok, A. Jamshidi, M. Kim, S. Dhuey, A. Lakhani, H. Choo, P. J. Schuck, S. Cabrini, A. M. Schwartzberg, J. Bokor, E. Yablonovitch, M. C. Wu, *Nano Lett.* **2011**, *11*, 2606.
[66] P. L. Stiles, J. A. Dieringer, N. C. Shah, R. R. Van Duyne, *Annu. Rev. Anal. Chem.* **2008**, *1*, 601.
[67] Y. Saito, T. Murakami, Y. Inouye, S. Kawata, *Chem. Lett.* **2005**, *34*, 920.
[68] B. Pettinger, B. Ren, G. Picardi, R. Schuster, G. Ertl, *Phys. Rev. Lett.* **2004**, *92*, 096101.
[69] C. C. Neacsu, J. Dreyer, N. Behr, M. B. Raschke, *Phys. Rev. B* **2006**, *73*, 193406.
[70] M. Sackrow, C. Stanciu, M. A. Lieb, A. J. Meixner, *ChemPhysChem* **2008**, *9*, 316.
[71] T. Deckert-Gaudig, V. Deckert, *Small* **2009**, *5*, 432.
[72] J. Stadler, T. Schmid, R. Zenobi, *Nano Lett.* **2010**, *10*, 4514.
[73] K. F. Domke, B. Pettinger, *ChemPhysChem* **2009**, *10*, 1794.
[74] R. Esteban, R. Vogelgesang, K. Kern, *Phys. Rev. B* **2007**, *75*, 195410.
[75] P. Biagioni, J. S. Huang, B. Hecht, *Rep. Prog. Phys.* **2012**, *75*, 024402.
[76] P. Muhlschlegel, H. J. Eisler, O. J. F. Martin, B. Hecht, D. W. Pohl, *Science* **2005**, *308*, 1607.
[77] P. J. Schuck, D. P. Fromm, A. Sundaramurthy, G. S. Kino, W. E. Moerner, *Phys. Rev. Lett.* **2005**, *94*, 017402.
[78] J. N. Farahani, D. W. Pohl, H. J. Eisler, B. Hecht, *Phys. Rev. Lett.* **2005**, *95*, 017402.
[79] Y. S. Zou, P. Steinvurzel, T. Yang, K. B. Crozier, *Appl. Phys. Lett.* **2009**, *94*, 171107.
[80] K. Iwami, T. Ono, M. Esashi, *J. Microelectromech. Syst.* **2006**, *15*, 1201.
[81] A. Weber-Bargioni, A. Schwartzberg, M. Schmidt, B. Harteneck, D. F. Ogletree, P. J. Schuck, S. Cabrini, *Nanotechnology* **2010**, *21*, 065306.
[82] A. Weber-Bargioni, A. Schwartzberg, M. Cornaglia, A. Ismach, J. J. Urban, Y. J. Pang, R. Gordon, J. Bokor, M. B. Salmeron, D. F. Ogletree, P. Ashby, S. Cabrini, P. J. Schuck, *Nano Lett.* **2011**, *11*, 1201.
[83] M. Fleischer, D. Zhang, K. Braun, S. Jager, R. Ehlich, M. Haffner, C. Stanciu, J. K. H. Horber, A. J. Meixner, D. P. Kern, *Nanotechnology* **2010**, *21*, 065301.
[84] T. W. Johnson, Z. J. Lapin, R. Beams, N. C. Lindquist, S. G. Rodrigo, L. Novotny, S.-H. Oh, *ACS Nano* **2012**, *6*, 9168.
[85] M. Fleischer, *Nanotechnol. Rev.* **2012**, *1*, 313.
[86] P. Biagioni, J. S. Huang, L. Duo, M. Finazzi, B. Hecht, *Phys. Rev. Lett.* **2009**, *102*, 256801.
[87] Z. Zhang, A. Weber-Bargioni, S. W. Wu, S. Dhuey, S. Cabrini, P. J. Schuck, *Nano Lett.* **2009**, *9*, 4505.
[88] A. McLeod, A. Weber-Bargioni, Z. Zhang, S. Dhuey, B. Harteneck, J. B. Neaton, S. Cabrini, P. J. Schuck, *Phys. Rev. Lett.* **2011**, *106*, 037402.
[89] A. Hartschuh, M. R. Beversluis, A. Bouhelier, L. Novotny, *Philos. Trans. R. Soc. London., Ser. A* **2004**, *362*, 807.
[90] N. Anderson, A. Hartschuh, L. Novotny, *Nano Lett.* **2007**, *7*, 577.
[91] A. Hartschuh, *Angew. Chem. Int. Ed.* **2008**, *47*, 8178.
[92] A. Hartschuh, H. N. Pedrosa, L. Novotny, T. D. Krauss, *Science* **2003**, *301*, 1354.
[93] F. De Angelis, G. Das, P. Candeloro, M. Patrini, M. Galli, A. Bek, M. Lazzarino, I. Maksymov, C. Liberale, L. C. Andreani, E. Di Fabrizio, *Nat. Nanotechnol.* **2010**, *5*, 67.
[94] J. Kurti, G. Kresse, H. Kuzmany, *Phys. Rev. B* **1998**, *58*, R8869.
[95] M. S. Dresselhaus, G. Dresselhaus, R. Saito, A. Jorio, *Phys. Rep.* **2005**, *409*, 47.
[96] M. S. Dresselhaus, G. Dresselhaus, A. Jorio, *J. Phys. Chem. C* **2007**, *111*, 17887.
[97] C. Fantini, A. Jorio, M. Souza, M. S. Strano, M. S. Dresselhaus, M. A. Pimenta, *Phys. Rev. Lett.* **2004**, *93*, 147406.
[98] C. Fantini, A. Jorio, M. Souza, R. Saito, G. G. Samsonidze, M. S. Dresselhaus, M. A. Pimenta, *Phys. Rev. B* **2005**, *72*, 085446.
[99] R. Saito, T. Takeya, T. Kimura, G. Dresselhaus, M. S. Dresselhaus, *Phys. Rev. B* **1999**, *59*, 2388.
[100] A. Rahmani, K. Sbai, H. Chadli, J. L. Sauvajol, *J. Phys.: Condens. Matter* **2008**, *20*, 015204.
[101] M. Mitra, S. Gopalakrishnan, *J. Appl. Phys.* **2007**, *101*, 114320.
[102] X. Zhang, W. Zhang, L. Liu, Z. X. Shen, *Chem. Phys. Lett.* **2003**, *372*, 497.
[103] G. Picardi, M. Chaigneau, R. Ossikovski, *Chem. Phys. Lett.* **2009**, *469*, 161.
[104] A. Rahmani, K. Sbai, H. Chadli, J. L. Sauvajol, *J. Phys.: Condens. Matter* **2009**, *21*, 045302.
[105] D. Li, R. Gordon, *Phys. Rev. A* **2010**, *82*, 041801(R).
[106] P. B. Catrysse, S. H. Fan, *Appl. Phys. Lett.* **2009**, *94*, 231111.
[107] M. J. Lockyear, A. P. Hibbins, J. R. Sambles, C. R. Lawrence, *Phys. Rev. Lett.* **2005**, *94*, 193902.
[108] Y. Poujet, J. Salvi, F. I. Baida, *Opt. Lett.* **2007**, *32*, 2942.
[109] R. de Waele, S. P. Burgos, A. Polman, H. A. Atwater, *Nano Lett.* **2009**, *9*, 2832.
[110] C. C. Neacsu, S. Berweger, R. L. Olmon, L. V. Saraf, C. Ropers, M. B. Raschke, *Nano Lett.* **2010**, *10*, 592.
[111] R. de Waele, S. P. Burgos, H. A. Atwater, A. Polman, *Opt. Express* **2010**, *18*, 12770.
[112] L. Neumann, Y. J. Pang, A. Houyou, M. L. Juan, R. Gordon, N. F. van Hulst, *Nano Lett.* **2011**, *11*, 355.
[113] Y. Wang, W. Srituravanich, C. Sun, X. Zhang, *Nano Lett.* **2008**, *8*, 3041.
[114] J. A. Matteo, D. P. Fromm, Y. Yuen, P. J. Schuck, W. E. Moerner, L. Hesselink, *Appl. Phys. Lett.* **2004**, *85*, 648.
[115] L. Wang, S. M. Uppuluri, E. X. Jin, X. F. Xu, *Nano Lett.* **2006**, *6*, 361.
[116] C. Ropers, C. C. Neacsu, T. Elsaesser, M. Albrecht, M. B. Raschke, C. Lienau, *Nano Lett.* **2007**, *7*, 2784.
[117] D. Sadiq, J. Shirdel, J. S. Lee, E. Selishcheva, N. Park, C. Lienau, *Nano Lett.* **2011**, *11*, 1609.
[118] M. Fleischer, A. Weber-Bargioni, M. V. P. Altoe, A. M. Schwartzberg, P. J. Schuck, S. Cabrini, D. P. Kern, *ACS Nano* **2011**, *5*, 2570.
[119] N. C. Lindquist, P. Nagpal, A. Lesuffleur, D. J. Norris, S.-H. Oh, *Nano Lett.* **2010**, *10*, 1369.
[120] W. Bao, M. Melli, N. Caselli, F. Riboli, D. S. Wiersma, M. Staffaroni, H. Choo, D. F. Ogletree, S. Aloni, J. Bokor, S. Cabrini, F. Intonti, M. B. Salmeron, E. Yablonovitch, P. J. Schuck, A. Weber-Bargioni, *Science* **2012**, *338*, 1317.
[121] M. Staffaroni, J. Conway, S. Vedantam, J. Tang, E. Yablonovitch, *Photonics Nanostruct.* **2012**, *10*, 166.

[122] P. Ginzburg, D. Arbel, M. Orenstein, *Opt. Lett.* **2006**, *31*, 3288.
[123] D. F. P. Pile, D. K. Gramotnev, *Appl. Phys. Lett.* **2006**, *89*, 041111
[124] D. K. Gramotnev, D. F. P. Pile, M. W. Vogel, X. Zhang, *Phys. Rev. B* **2007**, *75*, 035431.
[125] S. Vedantam, H. Lee, J. Tang, J. Conway, M. Staffaroni, E. Yablonovitch, *Nano Lett.* **2009**, *9*, 3447.
[126] E. Peytavit, J. F. Lampin, T. Akalin, L. Desplanque, *Electron. Lett.* **2007**, *43*, 73.
[127] X.-W. Chen, V. Sandoghdar, M. Agio, *Nano Lett.* **2009**, *9*, 3756.
[128] J. F. Wang, M. S. Gudiksen, X. F. Duan, Y. Cui, C. M. Lieber, *Science* **2001**, *293*, 1455.
[129] J. M. Bao, D. C. Bell, F. Capasso, J. B. Wagner, T. Martensson, J. Tragardh, L. Samuelson, *Nano Lett.* **2008**, *8*, 836.
[130] K. Cho, D. J. Ruebusch, M. H. Lee, J. H. Moon, A. C. Ford, R. Kapadia, K. Takei, O. Ergen, A. Javey, *Appl. Phys. Lett.* **2011**, *98*.
[131] A. Franceschetti, A. Zunger, *Phys. Rev. B* **2000**, *62*, R16287.
[132] S. A. Fischer, C. M. Isborn, O. V. Prezhdo, *Chem. Sci.* **2011**, *2*, 400.
[133] L. K. van Vugt, S. J. Veen, E. P. A. M. Bakkers, A. L. Roest, D. Vanmaekelbergh, *J. Am. Chem. Soc.* **2005**, *127*, 12357.
[134] E. Shafran, B. D. Mangum, J. M. Gerton, *Phys. Rev. Lett.* **2011**, *107*, 037403.
[135] J. J. Greffet, *Science* **2005**, *308*, 1561.